Double-blind decoupling of molecular rotation and high-order harmonic generation with a neural network

Siqi Sun,[1] Lixin He,[1,*] Chengqing Xu,[1] Yu Deng,[1] Pengfei Lan,[1,†] and Peixiang Lu[1,2]

[1]*Wuhan National Laboratory for Optoelectronics and School of Physics, Huazhong University of Science and Technology, Wuhan 430074, China*

[2]*Hubei Key Laboratory of Optical Information and Pattern Recognition, Wuhan Institute of Technology, Wuhan 430205, China*

(Received 23 October 2023; revised 16 January 2024; accepted 26 January 2024; published 8 March 2024)

High-order harmonic generation (HHG) through laser-molecule interaction provides a powerful means for detecting molecular structure and dynamics with subangström spatial and attosecond temporal resolution. However, accurately extracting molecular information from experimental harmonic spectra requires deconvolution of the angular average over the molecular rotational distribution, which is a challenging task due to the coherent nature of harmonic radiation. In this study we propose a deep-learning approach to disentangle the internal coupling between molecular alignment and single-molecule high-order harmonic radiation in experiments. With our method, the complex single-molecule dipole moments of high-order harmonics in both parallel and perpendicular directions, as well as the time-dependent molecular rotational distribution, can be simultaneously retrieved from the polarization-resolved angular distributions of HHG. From the retrieved harmonic dipole moments we can obtain comprehensive knowledge of the polarization states of the harmonics, including their ellipticity and helicity, without complicated experimental measurements. We demonstrate our method with two prototype molecules, N_2 and CO_2, in the experiment. Our approach provides an efficient way to disentangle single-molecule information from HHG experiments and will facilitate the study of molecular structure and dynamics imaging in complex polyatomic molecules.

DOI: 10.1103/PhysRevA.109.033105

I. INTRODUCTION

High-order harmonic generation (HHG) through laser-molecule interaction carries abundant information on the interacting system. This has stimulated the development of high-harmonic spectroscopy (HHS) as a powerful tool for accessing the structure and internal dynamics of molecules with subangström spatial resolution and attosecond temporal resolution [1–3] through a built-in pump-probe process underlying HHG described by the three-step model [4,5]. Recently, HHS has found widespread application in the detection of molecular structure and dynamics, including molecular orbital tomography [6,7], probing molecular vibration [8,9] and proton dynamics in molecules [10,11], decoding the underlying attosecond multielectron dynamics [12,13], and monitoring the attosecond charge migration in molecules [14–18]. These advancements have significantly enhanced our understanding of complex chemical and biological reactions [19].

A primary obstacle confronted by HHS is the extraction of individual molecular details from the harmonic emission, as the molecular-frame dynamics are encoded in the emission on the single-molecule level. In experimental settings, the HHG produced by a group of molecules is often an amalgamation of coherent results from numerous molecules that are oriented at different angles, resulting in the loss of single-molecule information. Although laser-induced molecular alignment partially addresses this concern, the obtained information remains blurred due to the inevitable imperfect molecular alignment in the experiment. Consequently, it is essential for HHS to disentangle the rotational coherence in the HHG experiment.

In the past few years, significant attempts have been undertaken to tackle the reconstruction of harmonic dipole moments at the single-molecule level from HHG experiments [20–23]. However, a common limitation in existing methodologies is the reliance on precise knowledge of the time-dependent molecular axis distributions, which is typically derived from some other independent measurements [24–29]. Errors in measuring molecular alignment thus can affect the accuracy of the reconstruction of the harmonic dipole moment. Besides, the commonly used traditional inverse problem-solving algorithms in previous works encounter great challenges, such as ill-posedness and high computational complexity, in extracting single-molecule information from harmonic signals due to the coherent nature of the HHG. To address these limitations, a more efficient reconstruction approach is necessary. This approach should enable the simultaneous reconstruction of both the molecular rotation and the harmonic dipole, without the need for prior knowledge of the time-dependent molecular axis distributions. We refer to this approach as a "double-blind reconstruction." On the other hand, in most previous works only one direction of the dipole moment (usually the parallel component) is considered. It is well known that elliptically polarized harmonics can be generated from the molecules [30,31], and a variety of techniques can be used to induce large ellipticity [32–34]. A full reconstruction of the harmonic

*helx_hust@hust.edu.cn
†pengfeilan@hust.edu.cn

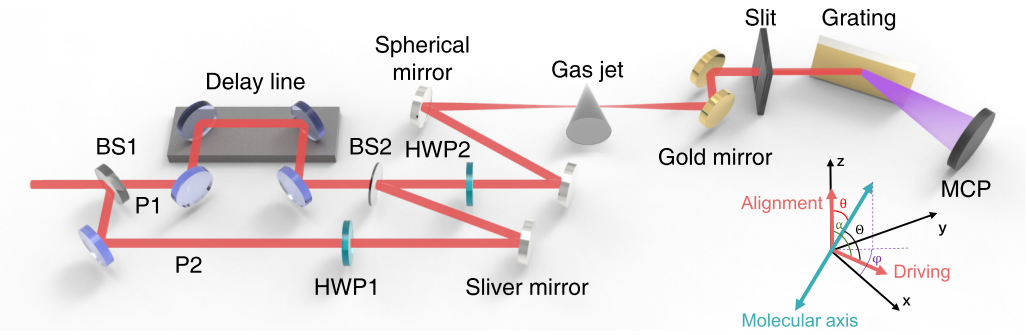

FIG. 1. Sketch of the experimental setup and the coordinate frame. BS: beam splitter, HWP: half-wave plate, MCP: microchannel plate.

dipole should include both the parallel and perpendicular components. It has been reported that the ultrafast nuclear motion [12] and electron dynamics [35] can be identified from the polarization-resolved high-harmonic spectra. Reconstruction of both the parallel and perpendicular harmonic dipole moments will assuredly strengthen the application ability of HHS, which, however, is still unattainable.

Deep learning algorithms offer a promising solution to these problems. By leveraging a data-driven approach and circumventing direct inverse problem solving, deep-learning algorithms can learn mapping relationships within the data, enabling signal reconstruction and information extraction with enhanced adaptability and superior performance. Deep learning has already demonstrated its utility in various applications, such as predicting high-harmonic flux [36], imaging molecular structures [37,38], pulse shape reconstruction from frequency-resolved optical gating or dispersion scan traces [39–41], simulating macroscopic high-order harmonic generation [42], retrieving the spectral phase of isolated attosecond x-ray pulses from streaking traces [43], and reconstructing band structures and pulse wave forms for high-harmonic spectroscopy in solids [44,45].

In this study we propose a deep-learning approach for the double-blind reconstruction of complex single-molecule harmonic dipole moments and the molecular rotational distribution from HHG signals. Our developed deep neural networks enable the complete retrieval of single-molecule harmonic dipole moments in both parallel and perpendicular directions, as well as the determination of the molecular rotational distribution from polarization-resolved angular distributions of HHG. The effectiveness of our method has been validated through tests conducted on theoretical and experimental data of N_2 and CO_2 molecules. Furthermore, the retrieved harmonic dipole moments provide comprehensive polarization information, including the ellipticity and helicity of the harmonics. In the future, polarization-resolved harmonic dipole moments will serve as a valuable resource for studying the structure and dynamics of polyatomic molecules.

II. EXPERIMENTAL SETUP AND THEORETICAL METHODS

A. Experimental setup

Figure 1 illustrates our experimental setup. To conduct our experiment, we employed a commercial Ti:sapphire laser system (Legend Elite-Duo, Coherent, Inc.) that generated 35-fs laser pulses with a wavelength of 800 nm and a repetition rate of 1 kHz. The output laser is divided into two beams (P1 and P2) by a beam splitter (BS1). Beam P2, polarized along the z direction, induces nonadiabatic alignment of the molecules in its direction, while beam P1 interacts with the aligned molecules to generate high-order harmonics. To adjust the molecular alignment angle α in the x-z plane, a half-wave plate (HWP1) is placed in the arm of P2, while a motorized delay line in the arm of P1 adjusts the time delay between P1 and P2. A second half-wave plate (HWP2) rotates the polarizations of P1 and P2 synchronously in their common path. We collinearly focused the two pulses into a supersonic gas jet, which was ejected from a 250-μm-diameter nozzle with a backing pressure of 0.8 bars, using a spherical mirror with a focal length of 250 mm. The gas jet is positioned 2 mm after the laser focus. The polarization of the high-order harmonics is analyzed by an extreme ultraviolet (EUV) polarizer, which comprises two gold mirrors at an incident angle of 45°. The polarizing angle β between the transmission axis (along the z axis) of the EUV polarizer and the polarization direction of P1 is adjusted by HWP2. Finally, high-order harmonics passing through the EUV polarizer are detected using a custom-made flat-field soft x-ray spectrometer consisting of an entrance slit (0.1 mm wide, 15 mm high), a flat-field grating (1200 grooves mm^{-1}), and a microchannel plate (MCP) backed with a phosphor screen. Spectral images on the phosphor screen are recorded by a CCD camera. In our experiment we measure the angular distributions of HHG from N_2 and CO_2 molecules around their half rotational revivals by scanning the molecular alignment angle α at three polarizing angles, $\beta = 0°$, 30°, and 60°, respectively.

B. Architecture of the neural network

In our study we have carefully designed two separate networks to address the retrieval of the single-molecule dipole moment and the molecular rotational distribution from the polarization-resolved angular distributions of HHG measured in the experiment. The network used to predict the complex dipole moment is illustrated in Fig. 2(a). It is based on a DenseNet-like architecture [46], which consists of five dense blocks and four transition blocks as the feature extractor, and two fully connected (FC) layers as the regressor. To address the complex-valued dipole moment, all the layers in the network are complex [47]. A gradient reversal layer

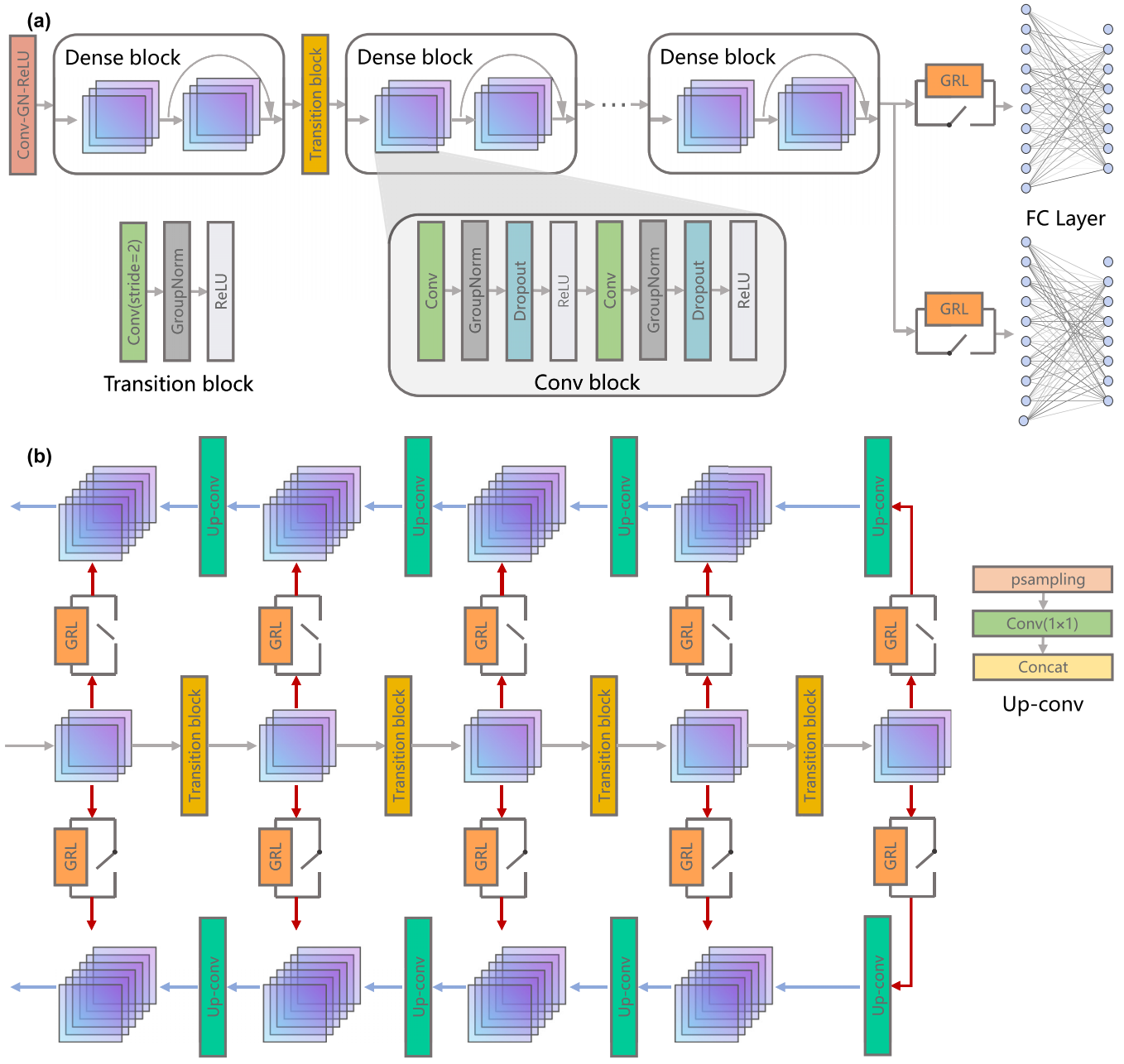

FIG. 2. (a) The architecture of the network used to predict the complex laser-induced dipole moment. The stacked purple squares represent a convolution block. The details of the convolution block and the transition block are provided in the subfigure. All layers in this network are complex-valued layers. (b) The architecture of the network used to predict the time-dependent molecular rotational distribution, with the details of the convolution block and the transition block the same as the network used for the complex dipole moment prediction. The details of the up-convolution layer are shown on the right.

(GRL) connects the feature extractor and the regressor. During forward propagation the GRL directly transports the output from the feature extractor to the regressor, while during backward propagation it inverts the gradient, which is a useful technique in adversarial training [48]. The network used to predict the time-dependent molecular rotational distribution is illustrated in Fig. 2(b). This network is based on the widely used U-net [49] architecture. In this work we use the down-sample branch as the feature extractor, which comprises five convolution blocks and four transition blocks. The up-sample branch is taken as the regressor, featuring four up-convolution layers and four convolution blocks. The neural layers in this network are standard real-valued layers, as the predicted time-dependent molecular rotational distribution is real. Note that one can also utilize a fusion architecture to address the above two reconstruction tasks within a unified model, while in our work, by employing separate networks we can effectively isolate the impact of their respective loss functions. This separation significantly simplifies the tuning and training process of our network, as well as the selection of appropriate hyperparameters, compared to using a multitasking architecture directly.

To train our networks, we have constructed the dataset in theory. The harmonic signal emitted by a group of partially aligned molecules is achieved through the coherent combination of individual molecular emissions, with each emission being weighted according to the rotational distribution of molecules. Mathematically, it can be expressed as the modulus square of the convolution of the time-dependent molecular rotational distribution $\rho(\theta, \phi, \tau)$ with the dipole moment of the single-molecule response $d_q(\Theta)$ [29,50,51]:

$$D_{\parallel/\perp,q}(\alpha, \tau) = \int_{\phi=0}^{2\pi} \int_{\theta=0}^{\pi} d_{\parallel/\perp,q}(\Theta)\rho(\theta, \phi, \tau) \sin\theta d\theta d\phi. \tag{1}$$

Here, q represents the harmonic order, while θ and ϕ denote the polar and azimuthal angles of the molecular axis in relation to the alignment laser's polarization. τ is the time delay between driving and alignment lasers. Θ corresponds to the polar angle within the molecular coordinate system, indicating the angle between the molecular axis and the driving laser's polarization. α is the polarization angle between the driving laser and the alignment laser (see Fig. 1). $\rho(\theta, \phi, \tau)$ is the molecular rotational distribution, which can be computed by solving the time-dependent Schrödinger equation under the rigid rotor approximation [52–55]. The single-molecule dipole moment $d_q(\Theta)$ is described by quantitative rescattering theory (QRS) [56], which has been successfully applied to model various strong-field phenomena, including high-energy above-threshold ionization (HATI), nonsequential double ionization (NSDI), and HHG [51,57,58]. QRS enables quantitative calculations that can be compared to experimental results [59], making it a valuable tool for studying these phenomena. The subscripts "$\parallel$ / $\perp$" denote the parallel/perpendicular components of the dipole moment.

The harmonic signals that pass through the EUV polarizer along the polarization angle β can be expressed as

$$\begin{aligned} I_{\beta,q}(\alpha, \tau) = &|D_{\parallel,q}(\alpha, \tau)\cos(\beta) + D_{\perp,q}(\alpha, \tau)\sin(\beta)|^2 \\ &+ e|D_{\parallel,q}(\alpha, \tau)\sin(\beta) + D_{\perp,q}(\alpha, \tau)\cos(\beta)|^2. \end{aligned} \tag{2}$$

Here e is the extinction ratio of the EUV polarizer, which is determined by measuring HHG from atoms with a linearly polarized laser (see Appendix A).

In our experiment we use the simulated signals $I_{\beta,q}(\alpha, \tau)$ with $\beta = 0^\circ$, 30°, and 60° as the input of our training. To conclude the order information, we employ a learnable embedding layer [60] to embed the order into a matrix with the same dimensions as $I_{\beta,q}(\alpha, \tau)$. The resulting embedding matrix is then added to the input signal to incorporate the order information. To generate our synthesized dataset, we have simulated $I_{\beta,q}(\alpha, \tau)$ by randomly selecting the intensity of the driving laser (ranging from 0.8×10^{14} to 2×10^{14} W/cm^2 for N_2 and from 0.6×10^{14} to 1.6×10^{14} W/cm^2 for CO_2), the intensity of the alignment laser (ranging from 1×10^{13} to 8×10^{13} W/cm^2), and the molecular rotational temperature (ranging from 20 to 300 K). In our training procedure we construct three datasets, the training set, validation set, and test set, by randomly selecting those parameters independently. The training set is used to train the model, while the validation set is used to tune hyperparameters and avoid overfitting. The test dataset remains separate from the other two datasets and is not exposed to the network during the training process. It is solely used to evaluate the performance of the trained model on previously unseen data. The dataset contains a total of 550,000 samples (including the training set, validation set, and test set), and the ratio of these three sets is 8:1:1.

C. Domain adaptation

We employ a domain adaptation method to enhance the generalization performance of our network on experimental signals. This technique allows us to improve the performance of a model on a target domain that has little or no labeled data by using the knowledge learned by the model from a related domain that has abundant labeled data. By transferring the learning from the source domain to the target domain, domain adaptation reduces the mismatch between the feature distributions of the two domains. This technique has been widely used in various fields such as image classification [48,61,62], key point detection [63], speech recognition [64,65], object detection [66,67], and photograph denoising [68].

One possible method for domain adaptation is adversarial learning, involving the training of a feature extractor and two regressors [63]. The feature extractor learns domain-invariant features that are useful for regression, while the regressors try to maximize the discrepancy of two outputs for the target domain and minimize the regression loss for the source domains based on the features. The three models are trained in an adversarial way, such that the feature extractor tries to fool the regressors by making the features indistinguishable across domains. In this way the feature extractor can learn features that are relevant for regression regardless of the domain.

In our network architecture, the regressors are connected to the feature extractor by a GRL to avoid the need for an alternate training procedure in adversarial learning [62]. A switch is connected in parallel to the GRL, which can be closed to shield the GRL during the propagation of data in the source domain to ensure minimal regression loss across the network. When the switch is open during the propagation of data in the target domain, the feature extractor minimizes the discrepancy while the regressor maximizes the discrepancy between the two regressors. This entire optimization procedure can be done simultaneously in a single framework. We utilized the absolute values of the difference between the two regressors' outputs, denoted as y_{1k} and y_{2k} for sample k in the target domain, as the discrepancy loss:

$$d(y_1, y_2) = \frac{1}{K}\sum_{k=1}^{K} |y_{1k} - y_{2k}|. \tag{3}$$

The regression loss used for the dipole network is defined as

$$\begin{aligned} \mathcal{L}(y_1, y_2, Y) = \frac{1}{N}\sum_{n=1}^{N} \Big\{ &\| |y_{1n} - Y_n| \|_2^2 + \| |y_{2n} - Y_n| \|_2^2 \\ &+ \lambda \Big[\| |e^{\arg(y_{1n})i} - e^{\arg(Y_n)i}| \|_2^2 \\ &+ \| |e^{\arg(y_{2n})i} - e^{\arg(Y_n)i}| \|_2^2 \Big] \Big\}. \end{aligned} \tag{4}$$

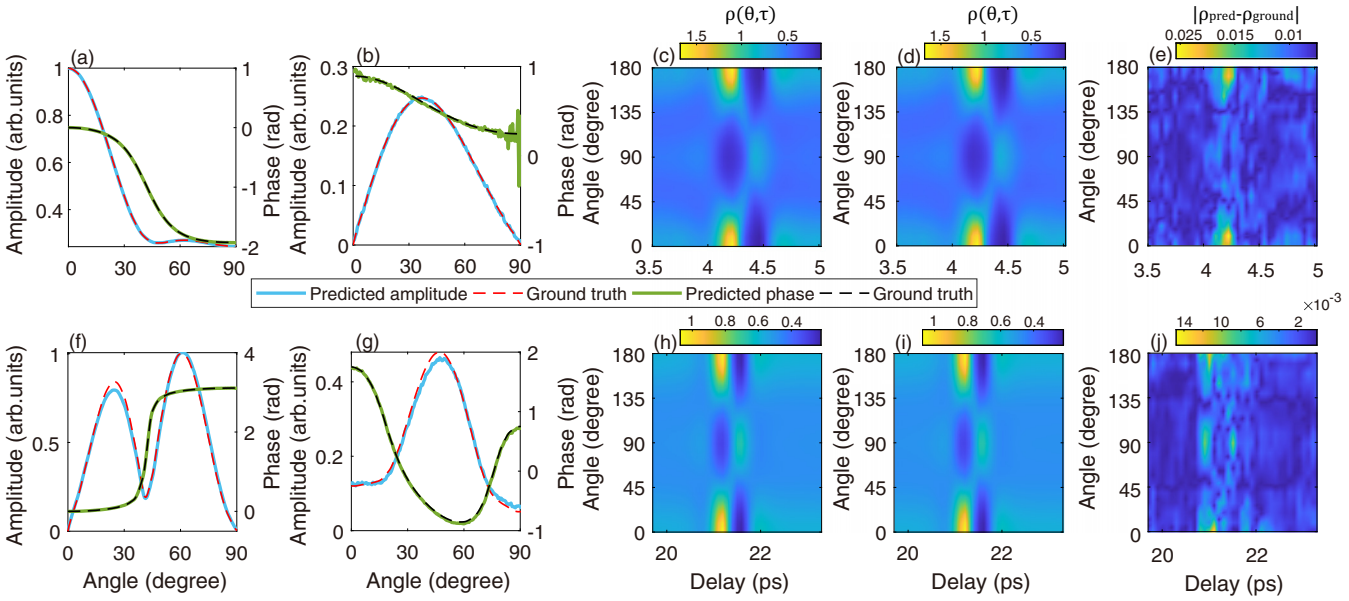

FIG. 3. (a) The predicted amplitudes (blue solid line) and phases (green solid line) of the laser-induced dipole moment in the parallel direction for N_2, respectively, while the red and black dashed lines are the ground truths. (b) Same as (a) but for the perpendicular direction. (c) Predicted time-dependent molecular rotational distribution. (d) The ground truth for the same prediction in (c). (e) The absolute difference between the prediction and ground truth of the molecular alignment distribution. (f)–(i) Same as (a)–(e) but for CO_2.

Here, y_{1n} and y_{2n} denote the output of the two regressors for sample n in the source domain, and Y_n denotes the label for sample n. λ is a real coefficient which is used to adjust the strength of the phase term in the loss function. The regression loss used for the alignment network is a transitional mean square error (MSE) loss.

During our training procedure, we first train the network with only the regression loss for a few epochs to warm up the network. The discrepancy loss is then added by multiplying a moderate weight to initiate the adversarial training. The regressors and feature extractor are trained individually using Adam optimization algorithms. In addition to the theoretically calculated training set, we also used the experimental data as the dataset for the target domain in order to train the network using the domain adaptation technique. For each gas (N_2 and CO_2), fifteen experimental images were sampled from five harmonic orders and three β values for training in every batch. The training process lasted 100 epochs. To handle the noisy background in the experimental data, one may employ the technique reported in [69] to enhance stability by generating synthetic noise within the dataset. However, in our approach we did not introduce synthetic background noise during training. This is because the domain adaptation technique we employed is capable of adapting to noisy backgrounds.

III. RESULTS AND DISCUSSION

We first demonstrate the performance of our network by using random samples from the test set. Figures 3(a) and 3(b) display the parallel and perpendicular components of the single-molecule dipole moments of H15 (solid lines) of N_2 predicted from a randomly selected HHG signal I_q with our network. As shown, the predicted dipole amplitude and phase for both components are in good agreement with the ground truths (dashed line), except for some phase shake in the perpendicular component near 90°. This is mainly because the amplitude of the perpendicular dipole moment is much smaller than that of the parallel component and is very close to zero near 90°. As our network predicts the real and imaginary parts of the dipole moment, this easily leads to phase instability. Figure 3(c) illustrates the corresponding time-dependent molecular rotational distribution ρ predicted with the same inputs as in Figs. 3(a) and 3(b). The absolute difference between the predicted molecular alignment distribution and the ground truth [see Fig. 3(d)] is shown in Fig. 3(e). The maximal absolute difference is about 0.025, indicating an excellent agreement between the prediction and the ground truth. We have also tested our network with a CO_2 molecule. The predictions by our network also agree with the ground truths, as shown in Figs. 3(f)–3(j). These results prove the accuracy and validity of our network. Additionally, in order to illustrate the overall performance of the network on the entire dataset, we have presented the mean loss of the networks for each gas and dataset in Table I. From Table I one can see that the loss values of the samples shown in Fig. 3 are close to those of different

TABLE I. The values of the loss function for each network and dataset.

	N_2		CO_2	
Dataset	Dipole	Alignment	Dipole	Alignment
Training set	0.0049	1.90×10^{-5}	0.0008	9.00×10^{-6}
Validation set	0.0041	1.90×10^{-5}	0.0007	9.00×10^{-6}
Test set	0.0041	1.95×10^{-5}	0.0008	9.00×10^{-6}
Samples in Fig. 3	0.0016	1.92×10^{-5}	0.0006	6.25×10^{-6}

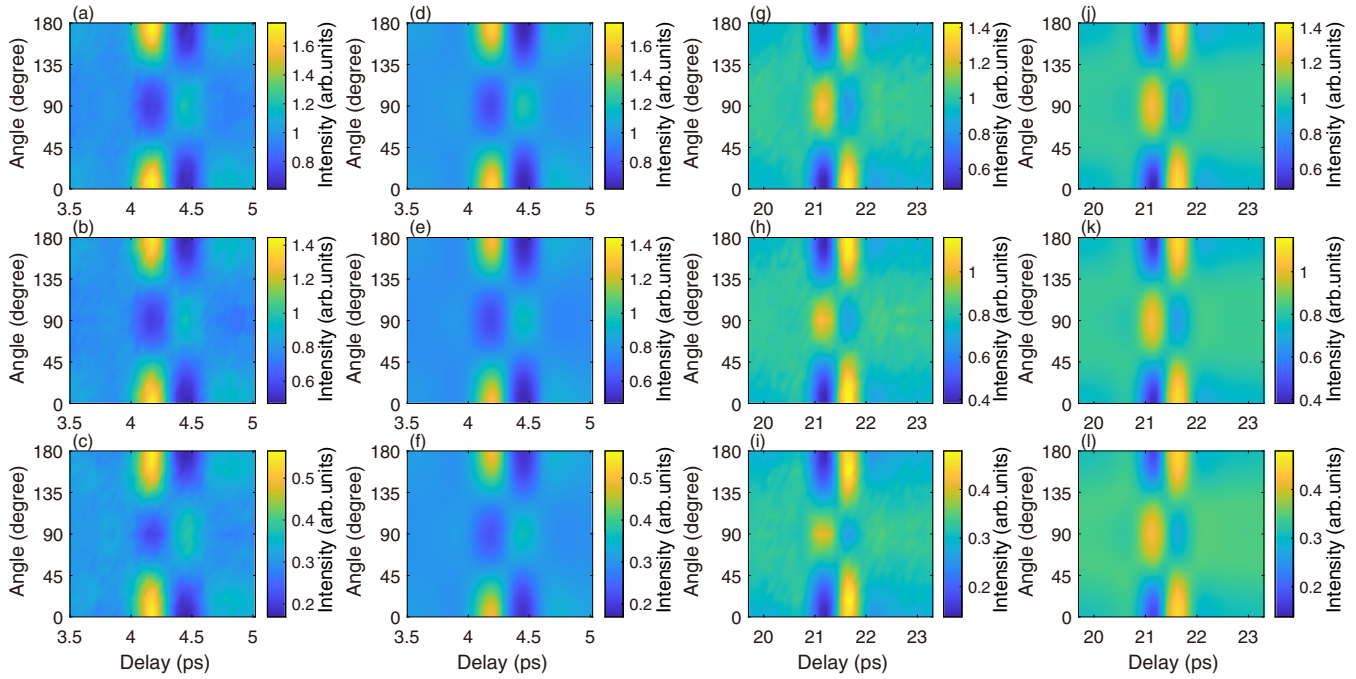

FIG. 4. (a)–(c) The experimental signals for $\beta = 0^\circ$, 30°, and 60° for H21 of N_2. (d)–(f) The reconstructed signals that are calculated using the retrievals from (a)–(c). (g)–(l) Same as (a)–(f) but for H23 of CO_2.

datasets. This result indicates that it is reasonable to evaluate the performance of the network with the samples in Fig. 3.

Next we demonstrate the application of our network to experimental data. The angular distribution of H21 measured near the half-rotational revival of N_2 with the polarizing angle β of 0°, 30°, and 60°, are shown in Figs. 4(a)–4(c). Note that the HHG signals measured in these three cases have been normalized by the isotropic result at $\beta = 0^\circ$. Using the measured HHG signals as input, we can obtain the single-molecule dipole moment for each order. Figures 5(a) and 5(b) show the extracted dipole amplitude (solid line) and phase (dashed line) of H17 along the parallel and perpendicular directions, respectively. Thanks to the domain adaptation technique employed, our model is able to compensate for the noise in the experimental data, resulting in only a minor fluctuation in the retrievals rather than complete destruction of the signal. In particular, the dipole moment in the perpendicular direction, which is much lower than that in the parallel direction, would have been entirely destroyed if the domain adaptation was not used (see Appendix C and Fig. 11). On the other hand, with our network, the time-dependent molecular rotational distribution ρ in our experiment can be simultaneously reconstructed [see Fig. 5(c)]. With the extracted single-molecule dipole moment and the molecular rotational distribution, we can recalculate the angular distribution of the considered harmonic according to Eqs. (1) and (2). As shown in Figs. 4(d)–4(f), the recalculated angular distributions of H21 of N_2 can well reproduce the experimental measurements in Figs. 4(a)–4(c). Such an agreement also indicates the accuracy of our network. We have also applied our network to other harmonic orders, e.g., H19 and H21 in Figs. 5(d)–5(f) and Figs. 5(g)–5(i), respectively. As shown, the retrieved molecular axis distributions are nearly the same for different harmonic orders. This result is consistent with the nature that HHG is a much faster process than molecular rotation; thus the rotational motion of the molecule during the femtosecond driving pulse is negligible.

Likewise, we have also applied our network to the experimental data of the CO_2 molecule. Figures 4(g)–4(l) display the measured signals of H23. Figure 6 shows the reconstructions for the harmonics H21–H25. One can see that the consistency of the reconstructed rotational distribution between different harmonic orders is also maintained [see Figs. 6(c), 6(f) and 6(i)] and the HHG signals recalculated, with the reconstructed dipole moment and molecular rotational distribution also agreeing well with the measurements [see Figs. 4(g)–4(l)].

Our deep-learning reconstructions have some advantages. First, from the measured polarization-resolved angular distributions of HHG, our network can accurately predict the complex single-molecule harmonic dipole moments along both the parallel and perpendicular directions. The comprehensive knowledge of the harmonic dipole moments thus enables a full reconstruction of the polarization states of the harmonics, which includes not only the absolute value of ellipticity but also the helicity (the sign of ellipticity) of the harmonic. In Figs. 7(a) and 7(b) we show the angle-dependent harmonic ellipticities obtained from the single-molecule harmonic dipole moments of N_2 and CO_2 retrieved above. As shown in Fig. 7(a), for N_2 the obtained ellipticity of each harmonic order presents a rapid change around 40°–60°. Especially, a minimum appears at H21 around 55° with an ellipticity reaching 0.35, which is consistent with previous experimental [30] and theoretical [70] studies. These phenomena arise from the phase jump in the single-molecule dipole moments as shown in Figs. 5(a), 5(d) and 5(g). Similar results are also observed in CO_2 molecules around 40° [see Fig. 7(b) and Figs. 6(a), 6(d) and 6(g)]. Note that for CO_2,

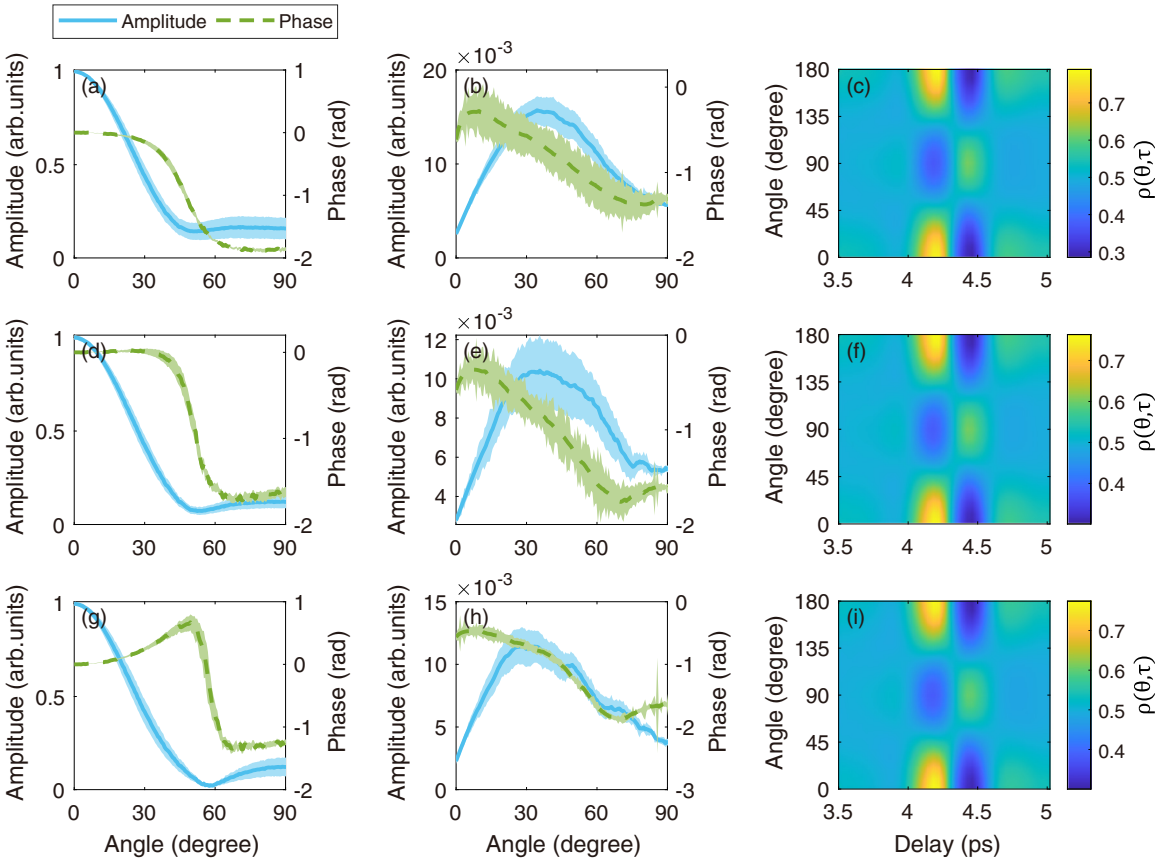

FIG. 5. (a) The retrieved amplitude (blue solid line) and phase (green dashed line) of laser-induced dipole moment in parallel direction for H17 of N_2. (b) Same as (a) but for the perpendicular direction. (c) The time-dependent molecular rotational distribution retrieved from the signals of H17. (d)–(f), (g)–(i) Same as (a)–(c) but for H19 and H21.

the accuracy of the harmonic ellipticity near 0° and 90° may be compromised, since the dipole amplitudes in both parallel and perpendicular directions are very close to 0. Furthermore, since the molecular rotational distribution is simultaneously obtained with our network, we can then estimate the harmonic ellipticity in our experiment by taking the rotational average effect into account. Solid lines in Figs. 7(c) and 7(d) show the harmonic ellipticities of H17-H25 obtained with our retrieved harmonic dipole moments and molecular rotational distribution for the alignment angle of 30° for N_2 and CO_2, respectively. For comparison, we have also directly measured the harmonic ellipticities for this alignment angle by scanning the polarizing angle β (see Appendix B). The results are shown as the circles in Figs. 7(c) and 7(d). One can see that the harmonic ellipticities estimated by our retrievals agree well with the experimental results. Here, it's worth mentioning that with our EUV polarizer we cannot obtain the harmonic helicity (the sign of the ellipticity). Figures 7(c) and 7(d) just plot the absolute values of the ellipticity. As in previous works, determining the harmonic helicity usually requires a complicated experimental setup, for instance, by using two pairs of EUV polarizers [71] or the magnetic circular dichroism measurement [72,73]. In contrast, with our deep-learning reconstruction method, the harmonic helicity in the experiment can be directly obtained [see Figs. 7(a) and 7(b)], which provides a more convenient way for such measurement.

Another potential application of our approach lies in its capacity to probe molecular structures and dynamics of complex polyatomic molecules. In most previous works the HHG measurement usually only contains one-dimensional information, which is inadequate for accessing molecules with increased degrees of freedom of nuclear and electron motions. Our approach presented here allows a full reconstruction of both the amplitude and phase of both the parallel and perpendicular components of the single-molecule dipole moments, which thus provides multidimensional data to gain a deep insight into the dynamics of molecules underlying the HHG process.

IV. CONCLUSION

In conclusion, we present a double-blind method for disentangling the internal coupling between molecular alignment and single-molecule high-order harmonic radiation in experiments by using neural networks. Our work utilizes a domain adaptation technique that improves the performance of the network on experimental signals by using end-to-end adversarial training. By competing between the feature extractor and regressors, the network is trained to make predictions using domain-invariant features, resulting in accurate and effective predictions of laser-induced dipole moments in both parallel and perpendicular directions and time-dependent molecular rotational distribution for the test set. We also test

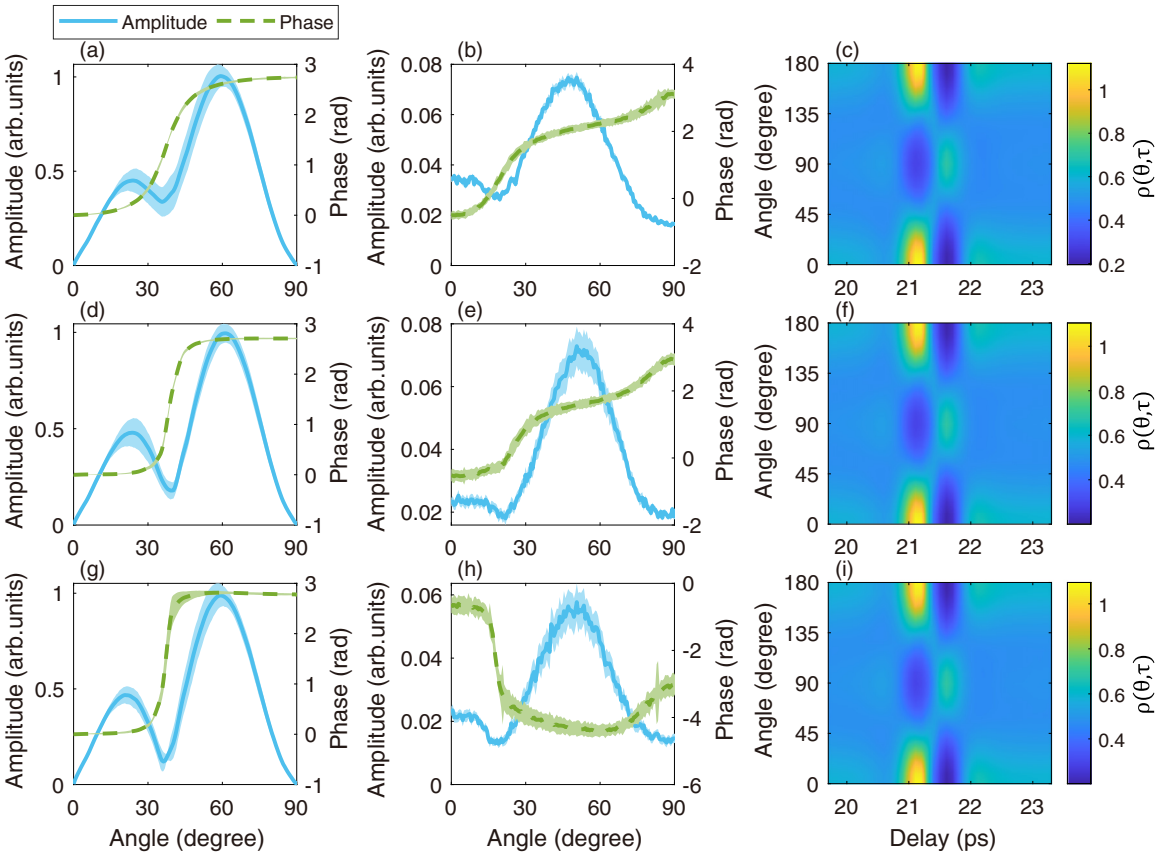

FIG. 6. (a) The retrieved amplitude (blue solid line) and phase (green dashed line) of laser-induced dipole moment in parallel direction for H21 of CO_2. (b) Same as (a) but for the perpendicular direction. (c) The time-dependent molecular rotational distribution retrieved from H21. (d)–(f), (g)–(i) Same as (a)–(c) but for H23 and H25.

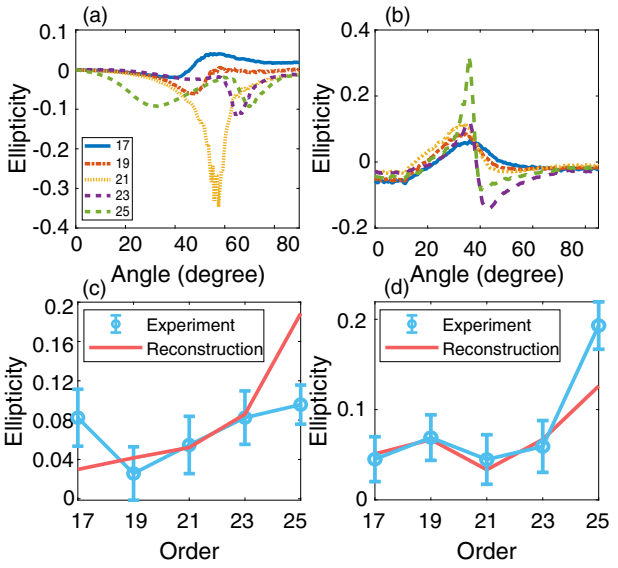

FIG. 7. Reconstructions of harmonic ellipticities of N_2 and CO_2. (a) Reconstructed single-molecule angle-dependent harmonic ellipticities of H17, H19, H21, H23, and H25 for N_2. (b) Same as (a) but for CO_2. (c) The experiment (blue circles) and reconstructed (red lines) ellipticities with the rotational average effect of H17, H19, H21, H23, and H25 for N_2. (d) Same as (c) but for CO_2.

our method using experimental data for N_2 and CO_2. The reconstructed signals show good consistency with the measured signals. Moreover, our method enables the reconstruction of the polarization state of the harmonic, including the ellipticity and the helicity, providing comprehensive single-molecule harmonic information. This method can be easily extended to other molecules by training the network with the corresponding dataset. Specifically, for asymmetric molecules such as CO, the dataset of the harmonic dipole moment can also be built using the QRS theory. But for the molecular rotational distribution, it requires molecular orientation in both experiment and theory. In the future our method can provide a tool for the study of molecular structures and dynamics of complex polyatomic molecules, and to facilitate the development of new applications in ultrafast science and technology.

ACKNOWLEDGMENTS

The authors gratefully acknowledge Yanqing He for helping to complete the experiment and highly insightful discussion of this research. This work is supported by the National Key Research and Development Program of China (Grants No. 2023YFA1406800 and No. 2019YFA0308300), the National Natural Science Foundation of China (Grants No. 91950202, No. 12225406, No. 12074136, No. 12021004, and No. 11934006), and the Natural Science Foundation of Hubei Province (No. 2021CFB330). The computing work in

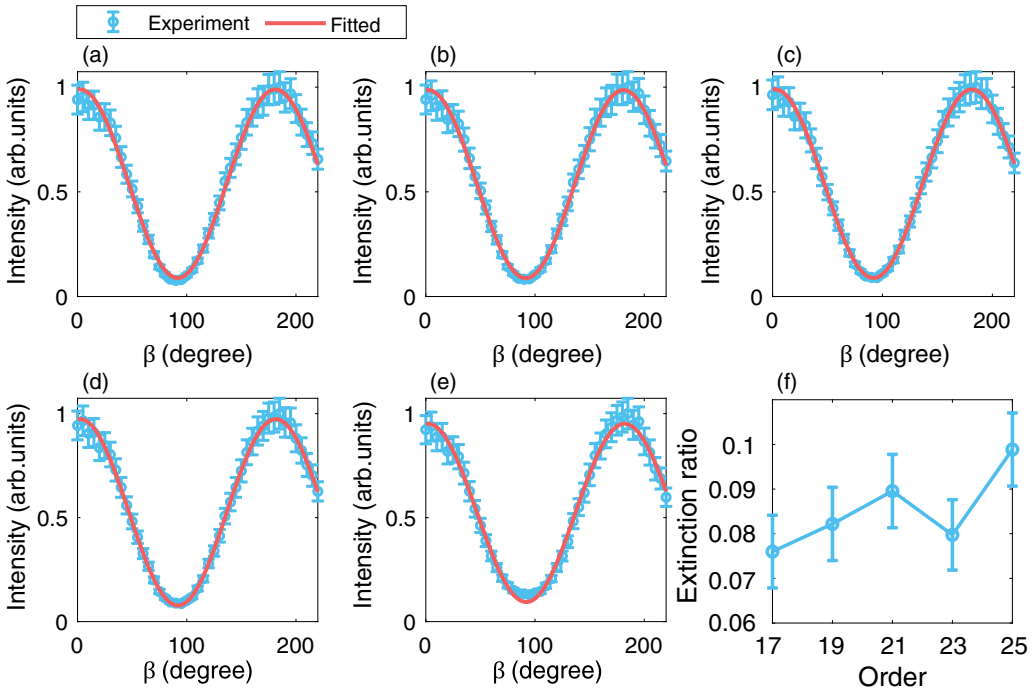

FIG. 8. (a)–(e) Experimental signals of H17–H25 of Ar measured as a function of the polarization angle β. Solid lines are the fitting results with Eq. (A1). (f) The extinction ratios of H17–H25 extracted from (a)–(e).

this paper is supported by the Public Service Platform of High-Performance Computing provided by the Network and Computing Center of HUST.

APPENDIX A: EXTINCTION RATIO OF THE EUV POLARIZER

In order to determine the extinction ratio of the EUV polarizer used in our experiment, we measured the HHG signal from Ar atoms with a linearly polarized laser. Specifically, we measured the HHG intensities passing through the EUV polarizer for various β. The corresponding results are presented as blue circles in Figs. 8(a)–8(e) for H17, H19, H21, H23, and H25. Based on the Malus law, the output harmonic intensity after passing through the EUV reflective polarizer is formulated as [30,74,75]

$$I(\beta) = a\cos[2(\beta - \phi)] + c, \tag{A1}$$

where a and c are positive constants, and ϕ is the angle of the major axes of the HHG ellipse, which is also a constant. To extract the extinction ratio, we fit the measure signals with Eq. (A1) [red lines in Figs. 8(a)–8(e)]. The intensity ratio between the minimum and maximum output harmonic intensity reads

$$R = \frac{I_{\min}}{I_{\max}} = \frac{R_s I_{\text{minor}} + R_p I_{\text{major}}}{R_p I_{\text{minor}} + R_s I_{\text{major}}}, \tag{A2}$$

where I_{major} and I_{minor} are the intensities on the major and minor axes of the HHG ellipse, respectively; R_s and R_p are the reflectivity of the s- and p-polarized harmonics, as the HHG emission from Ar atoms is purely linearly polarized, which means $I_{\text{minor}} = 0$. We can then obtain the extinction ratio $e = R_p/R_s$ by dividing the minimum value by the maximum value of the output harmonic intensity. The obtained extinction ratios for different harmonic orders are shown in Fig. 8(f).

APPENDIX B: EXPERIMENTAL MEASUREMENT OF HARMONIC ELLIPTICITY WITH THE EUV POLARIZER

To evaluate the polarization-resolved harmonic dipoles retrieved by our networks, we have measured the ellipticity of harmonics generated from N_2 and CO_2 with the alignment angle of 30° by scanning the polarization angle β. Figure 9 displays the experimental signals for H17, H19, H21, H23, and H25 for N_2 and CO_2. By fitting the measured HHG signals with Eq. (S1) (see red solid lines in Fig. 9), we can obtain the intensity ratio R. The harmonic ellipticity then can be obtained by

$$\varepsilon = \sqrt{\frac{R - e}{1 - eR}}. \tag{B1}$$

The measured harmonic ellipticities for N_2 and CO_2 are shown in Figs. 7(c) and 7(d), which are in good agreement with the results calculated with our retrievals.

APPENDIX C: AN EXAMPLE FOR NOT USING DOMAIN ADAPTATION

For a better understanding of the impact of the domain adaptation, we conducted network training without employing the domain adaptation. The obtained results predicted from the HHG signals in Figs. 4(a)–4(c) are presented in Fig. 10. It is evident that the perpendicular component of the dipole moment [see Fig. 10(b)] differs significantly from that shown in Fig. 5(h), which is approximately four times larger. Fur-

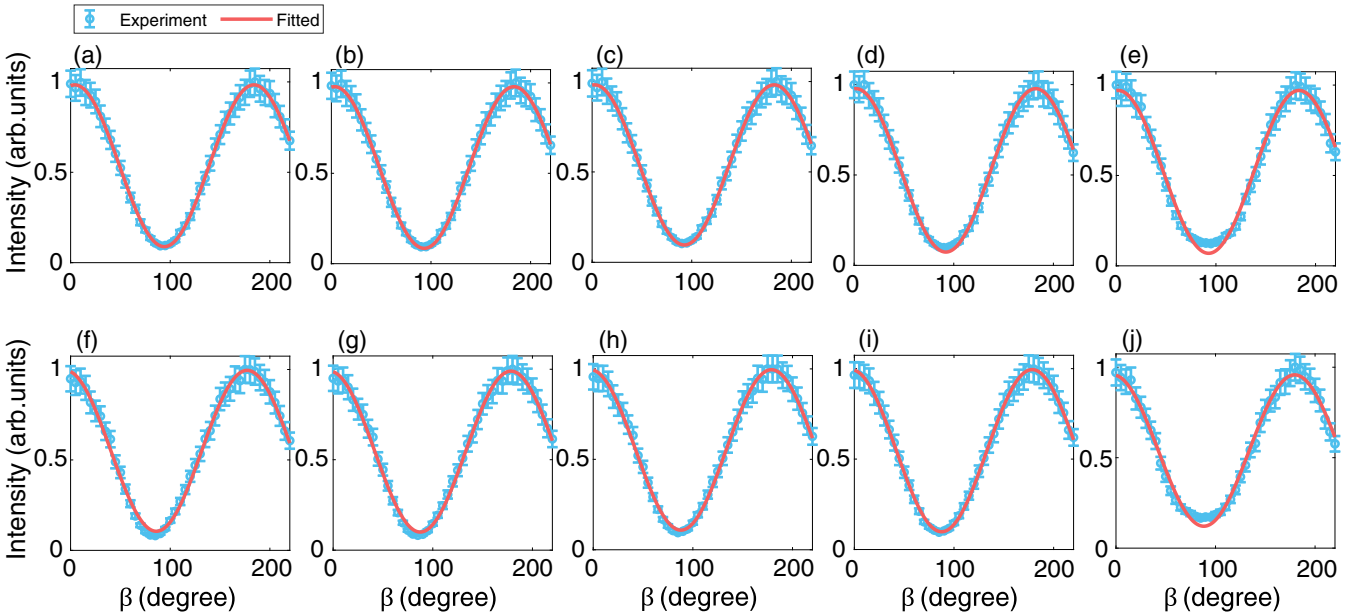

FIG. 9. (a)–(e) Experimental signals of H17–H25 of N_2 measured as a function of the polarization angle for the alignment angle of 30°. Solid lines are the fitting results with Eq. (A1). (f)–(j) Same as (a)–(e) but for CO_2 molecule.

thermore, the rotational distribution in Fig. 10(c) also exhibits a significant difference compared to Fig. 5(i), with absolute difference up to 0.56 [see Fig. 10(d)]. We also calculated the HHG signals with the retrieved harmonic dipole moment and alignment distribution in Fig. 10. The results are shown in Figs. 11(a)–11(c). As shown in Figs. 11(d)–11(f), which present the absolute difference between the reconstructed signals and the real experimental signals, a clear mismatch between them is observed. This result indicates the critical role of domain adaptation during network training.

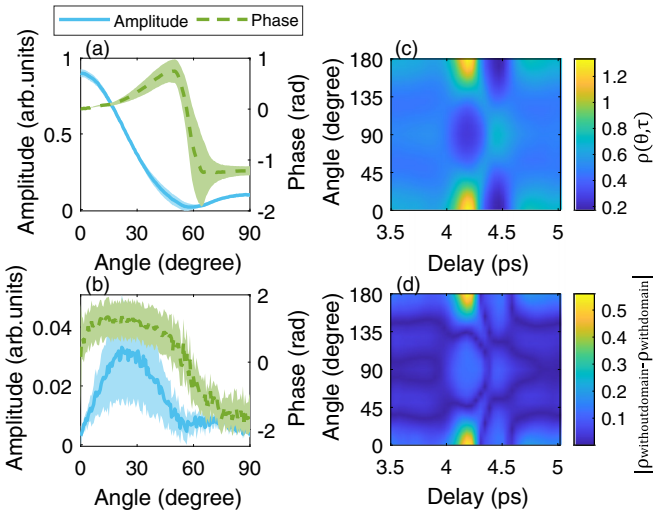

FIG. 10. (a) The amplitude (blue solid line) and phase (green dashed line) of laser-induced dipole moment in parallel direction retrieved by the network trained without domain adaptation. (b) Same as (a) but for the perpendicular direction. (c) The corresponding time-dependent molecular rotational distribution. (d) The absolute difference between the retrieved molecular rotational distribution obtained by using the network without and with domain adaptation.

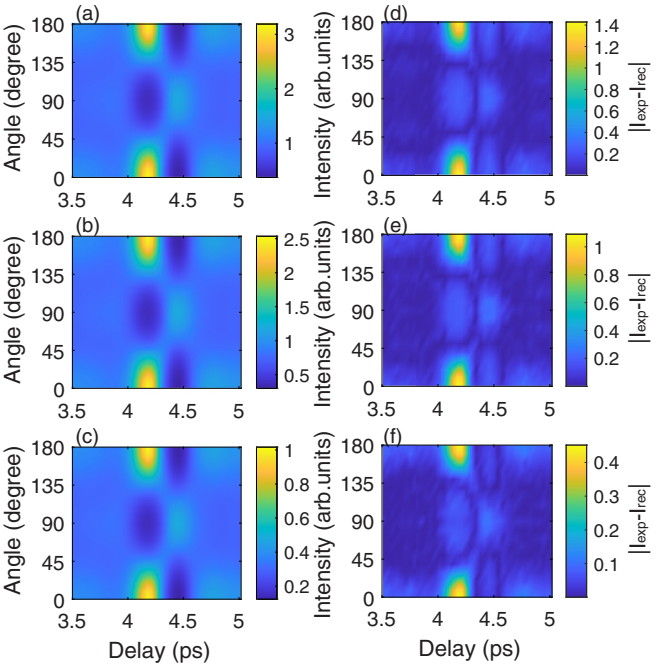

FIG. 11. (a)–(c) The HHG signals for $\beta = 0°$, 30°, and 60° reconstructed using the retrievals in Figs. 10(a)–10(c). (d)–(f) The absolute difference between the reconstructed signals and the experimental signals.

[1] P. B. Corkum, Recollision physics, Phys. Today **64**, 36 (2011).

[2] F. Calegari, G. Sansone, S. Stagira, C. Vozzi, and M. Nisoli, Advances in attosecond science, J. Phys. B: At., Mol. Opt. Phys. **49**, 062001 (2016).

[3] L. Li, P. Lan, X. Zhu, and P. Lu, High harmonic generation in solids: Particle and wave perspectives, Rep. Prog. Phys. **86**, 116401 (2023).

[4] P. B. Corkum, Plasma perspective on strong field multiphoton ionization, Phys. Rev. Lett. **71**, 1994 (1993).

[5] M. Lewenstein, P. Balcou, M. Y. Ivanov, A. L'Huillier, and P. B. Corkum, Theory of high-harmonic generation by low-frequency laser fields, Phys. Rev. A **49**, 2117 (1994).

[6] J. Itatani, J. Levesque, D. Zeidler, H. Niikura, H. Pépin, J. C. Kieffer, P. B. Corkum, and D. M. Villeneuve, Tomographic imaging of molecular orbitals, Nature (London) **432**, 867 (2004).

[7] C. Vozzi, M. Negro, F. Calegari, G. Sansone, M. Nisoli, S. De Silvestri, and S. Stagira, Generalized molecular orbital tomography, Nat. Phys. **7**, 822 (2011).

[8] A. Ferré, D. Staedter, F. Burgy, M. Dagan, D. Descamps, N. Dudovich, S. Petit, H. Soifer, V. Blanchet, and Y. Mairesse, High-order harmonic transient grating spectroscopy of SF6 molecular vibrations, J. Phys. B: At., Mol. Opt. Phys. **47**, 124023 (2014).

[9] L. He, Q. Zhang, P. Lan, W. Cao, X. Zhu, C. Zhai, F. Wang, W. Shi, M. Li, X.-B. Bian *et al.*, Monitoring ultrafast vibrational dynamics of isotopic molecules with frequency modulation of high-order harmonics, Nat. Commun. **9**, 1108 (2018).

[10] S. Baker, J. S. Robinson, C. A. Haworth, H. Teng, R. A. Smith, C. C. Chirilă, M. Lein, J. W. G. Tisch, and J. P. Marangos, Probing proton dynamics in molecules on an attosecond time scale, Science **312**, 424 (2006).

[11] P. Lan, M. Ruhmann, L. He, C. Zhai, F. Wang, X. Zhu, Q. Zhang, Y. Zhou, M. Li, M. Lein *et al.*, Attosecond probing of nuclear dynamics with trajectory-resolved high-harmonic spectroscopy, Phys. Rev. Lett. **119**, 033201 (2017).

[12] O. Smirnova, Y. Mairesse, S. Patchkovskii, N. Dudovich, D. Villeneuve, P. Corkum, and M. Y. Ivanov, High harmonic interferometry of multi-electron dynamics in molecules, Nature (London) **460**, 972 (2009).

[13] A. Shiner, B. Schmidt, C. Trallero-Herrero, H. J. Wörner, S. Patchkovskii, P. B. Corkum, J. Kieffer, F. Légaré, and D. Villeneuve, Probing collective multi-electron dynamics in xenon with high-harmonic spectroscopy, Nat. Phys. **7**, 464 (2011).

[14] L. He, S. Sun, P. Lan, Y. He, B. Wang, P. Wang, X. Zhu, L. Li, W. Cao, P. Lu, and C. D. Lin, Filming movies of attosecond charge migration in single molecules with high harmonic spectroscopy, Nat. Commun. **13**, 4595 (2022).

[15] P. M. Kraus, B. Mignolet, D. Baykusheva, A. Rupenyan, L. Horný, E. F. Penka, G. Grassi, O. I. Tolstikhin, J. Schneider, F. Jensen, L. B. Madsen, A. D. Bandrauk, F. Remacle, and H. J. Wörner, Measurement and laser control of attosecond charge migration in ionized iodoacetylene, Science **350**, 790 (2015).

[16] J. Liang, Y. Zhou, Y. Liao, W.-C. Jiang, M. Li, and P. Lu, Direct visualization of deforming atomic wavefunction in ultraintense high-frequency laser pulses, Ultrafast Science **2022**, 2022/9842716 (2022).

[17] Y. Huang, J. Zhao, Z. Shu, Y. Zhu, J. Liu, W. Dong, X. Wang, Z. Lü, D. Zhang, J. Yuan, J. Chen, and Z. Zhao, Ultrafast hole deformation revealed by molecular attosecond interferometry, Ultrafast Science **2021**, 9837107 (2021).

[18] L. He, Y. He, S. Sun, E. Goetz, A.-T. Le, X. Zhu, P. Lan, P. Lu, and C.-D. Lin, Attosecond probing and control of charge migration in carbon-chain molecule, Adv. Photonics **5**, 056001 (2023).

[19] F. Remacle and R. D. Levine, An electronic time scale in chemistry, Proc. Natl. Acad. Sci. USA **103**, 6793 (2006).

[20] X. Wang, A.-T. Le, Z. Zhou, H. Wei, and C. D. Lin, Theory of retrieving orientation-resolved molecular information using time-domain rotational coherence spectroscopy, Phys. Rev. A **96**, 023424 (2017).

[21] B. Wang, Y. He, X. Zhao, L. He, P. Lan, P. Lu, and C. D. Lin, Retrieval of full angular-and energy-dependent complex transition dipoles in the molecular frame from laser-induced high-order harmonic signals with aligned molecules, Phys. Rev. A **101**, 063417 (2020).

[22] S. Sun, Y. He, L. He, J. Hu, P. Lan, and P. Lu, Iterative projection algorithm for retrieval of angle-resolved single-molecule dipoles from high-harmonic spectra, Phys. Rev. A **107**, 033105 (2023).

[23] L. He, X. Zhu, W. Cao, P. Lan, and P. Lu, Attosecond spectroscopy for filming the ultrafast movies of atoms, molecules and solids, Chin. Phys. B **31**, 123301 (2022).

[24] K. Yoshii, G. Miyaji, and K. Miyazaki, Measurement of molecular rotational temperature in a supersonic gas jet with high-order harmonic generation, Opt. Lett. **34**, 1651 (2009).

[25] Y. He, L. He, P. Lan, B. Wang, L. Li, X. Zhu, W. Cao, and P. Lu, Direct imaging of molecular rotation with high-order-harmonic generation, Phys. Rev. A **99**, 053419 (2019).

[26] T. Hornung, H. Skenderović, K.-L. Kompa, and M. Motzkus, Prospect of temperature determination using degenerate four-wave mixing with sub-20 fs pulses, J. Raman Spectrosc. **35**, 934 (2004).

[27] P. Wang, L. He, Y. He, J. Hu, S. Sun, P. Lan, and P. Lu, Rotational echo spectroscopy for accurate measurement of molecular alignment, Opt. Lett. **47**, 1033 (2022).

[28] T. Lang, M. Motzkus, H. Frey, and P. Beaud, High resolution femtosecond coherent anti-Stokes Raman scattering: Determination of rotational constants, molecular anharmonicity, collisional line shifts, and temperature, J. Chem. Phys. **115**, 5418 (2001).

[29] Y. He, L. He, P. Wang, B. Wang, S. Sun, R. Liu, B. Wang, P. Lan, and P. Lu, Measuring the rotational temperature and pump intensity in molecular alignment experiments via high harmonic generation, Opt. Express **28**, 21182 (2020).

[30] X. Zhou, R. Lock, N. Wagner, W. Li, H. C. Kapteyn, and M. M. Murnane, Elliptically polarized high-order harmonic emission from molecules in linearly polarized laser fields, Phys. Rev. Lett. **102**, 073902 (2009).

[31] A.-T. Le, R. R. Lucchese, and C. D. Lin, Polarization and ellipticity of high-order harmonics from aligned molecules generated by linearly polarized intense laser pulses, Phys. Rev. A **82**, 023814 (2010).

[32] R. Shao, C. Zhai, Y. Zhang, N. Sun, W. Cao, P. Lan, and P. Lu, Generation of isolated circularly polarized attosecond pulses by three-color laser field mixing, Opt. Express **28**, 15874 (2020).

[33] W. Li, X. Zhu, P. Lan, and P. Lu, Elliptically polarized attosecond pulse generation by corotating bicircular laser fields, Phys. Rev. A **106**, 043115 (2022).

[34] C. Zhai, X. Zhu, J. Long, R. Shao, Y. Zhang, L. He, Q. Tang, Y. Li, P. Lan, B. Yu *et al.*, Generation of elliptically polarized attosecond pulses in mixed gases, Phys. Rev. A **103**, 033114 (2021).

[35] Y. Mairesse, J. Higuet, N. Dudovich, D. Shafir, B. Fabre, E. Mével, E. Constant, S. Patchkovskii, Z. Walters, M. Y. Ivanov *et al.*, High harmonic spectroscopy of multichannel dynamics in strong-field ionization, Phys. Rev. Lett. **104**, 213601 (2010).

[36] A. M. M. Gherman, K. Kovács, M. V. Cristea, and V. Toşa, Artificial neural network trained to predict high-harmonic flux, Appl. Sci. **8**, 2106 (2018).

[37] X. Liu, K. Amini, A. Sanchez, B. Belsa, T. Steinle, and J. Biegert, Machine learning for laser-induced electron diffraction imaging of molecular structures, Commun. Chem. **4**, 1 (2021).

[38] N. I. Shvetsov-Shilovski and M. Lein, Transfer learning, alternative approaches, and visualization of a convolutional neural network for retrieval of the internuclear distance in a molecule from photoelectron momentum distributions, Phys. Rev. A **107**, 033106 (2023).

[39] T. Zahavy, A. Dikopoltsev, D. Moss, G. I. Haham, O. Cohen, S. Mannor, and M. Segev, Deep learning reconstruction of ultrashort pulses, Optica **5**, 666 (2018).

[40] S. Kleinert, A. Tajalli, T. Nagy, and U. Morgner, Rapid phase retrieval of ultrashort pulses from dispersion scan traces using deep neural networks, Opt. Lett. **44**, 979 (2019).

[41] I. Tóth, A. M. M. Gherman, K. Kovács, W. Cho, H. Yun, and V. Toşa, Reconstruction of femtosecond laser pulses from frog traces by convolutional neural networks, Photonics **10**, 1195 (2023).

[42] J. M. Pablos-Marín, J. Serrano, and C. Hernández-García, Simulating macroscopic high-order harmonic generation driven by structured laser beams using artificial intelligence, Comput. Phys. Commun. **291**, 108823 (2023).

[43] J. White and Z. Chang, Attosecond streaking phase retrieval with neural network, Opt. Express **27**, 4799 (2019).

[44] N. D. Klimkin, A. Jiménez-Galán, R. E. F. Silva, and M. Ivanov, Deep neural networks for high harmonic spectroscopy in solids, arXiv:2106.08638.

[45] L. Li, P. Lan, L. He, W. Cao, Q. Zhang, and P. Lu, Determination of electron band structure using temporal interferometry, Phys. Rev. Lett. **124**, 157403 (2020).

[46] G. Huang, Z. Liu, L. Van Der Maaten, and K. Q. Weinberger, Densely connected convolutional networks, in *2017 IEEE Conference on Computer Vision and Pattern Recognition (CVPR)* (IEEE, New York, 2017), pp. 2261–2269.

[47] C. Trabelsi, O. Bilaniuk, Y. Zhang, D. Serdyuk, S. Subramanian, J. F. Santos, S. Mehri, N. Rostamzadeh, Y. Bengio, and C. J. Pal, Deep complex networks, *6th International Conference on Learning Representations, ICLR 2018* (OpenReview.net, Vancouver, BC, Canada), pp. 1–19.

[48] Y. Ganin and V. Lempitsky, Unsupervised domain adaptation by backpropagation, in *Proceedings of the 32nd International Conference on Machine Learning* (JMLR, Cambridge MA, 2015), pp. 1180–1189.

[49] O. Ronneberger, P. Fischer, and T. Brox, U-Net: Convolutional networks for biomedical image segmentation, in *Medical Image Computing and Computer-Assisted Intervention–MICCAI 2015*, Lecture Notes in Computer Science, edited by N. Navab, J. Hornegger, W. M. Wells, and A. F. Frangi (Springer International Publishing, Cham, 2015), pp. 234–241.

[50] L. He, P. Lan, A.-T. Le, B. Wang, B. Wang, X. Zhu, P. Lu, and C. D. Lin, Real-time observation of molecular spinning with angular high-harmonic spectroscopy, Phys. Rev. Lett. **121**, 163201 (2018).

[51] A.-T. Le, R. R. Lucchese, S. Tonzani, T. Morishita, and C. D. Lin, Quantitative rescattering theory for high-order harmonic generation from molecules, Phys. Rev. A **80**, 013401 (2009).

[52] S. Fleischer, Y. Khodorkovsky, E. Gershnabel, Y. Prior, and I. S. Averbukh, Molecular alignment induced by ultrashort laser pulses and its impact on molecular motion, Isr. J. Chem. **52**, 414 (2012).

[53] I. Simkó, K. Chordiya, A. G. Császár, M. U. Kahaly, and T. Szidarovszky, A quantum-chemical perspective on the laser-induced alignment and orientation dynamics of the CH3X (X= F, Cl, Br, I) molecules, J. Comput. Chem. **43**, 519 (2022).

[54] T. Szidarovszky, M. Jono, and K. Yamanouchi, LIMAO: Cross-platform software for simulating laser-induced alignment and orientation dynamics of linear-, symmetric- and asymmetric tops, Comput. Phys. Commun. **228**, 219 (2018).

[55] X. Ren, V. Makhija, and V. Kumarappan, Multipulse three-dimensional alignment of asymmetric top molecules, Phys. Rev. Lett. **112**, 173602 (2014).

[56] C.-D. Lin, A.-T. Le, C. Jin, and H. Wei, *Attosecond and Strong-Field Physics: Principles and Applications* (Cambridge University Press, Cambridge, England, 2018).

[57] C. Lin, A.-T. Le, C. Jin, and H. Wei, Elements of the quantitative rescattering theory, J. Phys. B: At., Mol. Opt. Phys. **51**, 104001 (2018).

[58] A.-T. Le, R. R. Lucchese, and C. D. Lin, Quantitative rescattering theory of high-order harmonic generation for polyatomic molecules, Phys. Rev. A **87**, 063406 (2013).

[59] C. Lin, A.-T. Le, Z. Chen, T. Morishita, and R. Lucchese, Strong-field rescattering physics—Self-imaging of a molecule by its own electrons, J. Phys. B: At., Mol. Opt. Phys. **43**, 122001 (2010).

[60] A. Vaswani, N. Shazeer, N. Parmar, J. Uszkoreit, L. Jones, A. N. Gomez, L. Kaiser, and I. Polosukhin, Attention is all you need, in *Advances in Neural Information Processing Systems*, Vol. 30 (Curran Associates, Inc., Red Hook, NY, 2017).

[61] M. Ghifary, W. B. Kleijn, M. Zhang, D. Balduzzi, and W. Li, Deep Reconstruction-classification networks for unsupervised domain adaptation, in *Computer Vision–ECCV 2016*, Lecture Notes in Computer Science, edited by B. Leibe, J. Matas, N. Sebe, and M. Welling (Springer International Publishing, Cham, 2016), pp. 597–613.

[62] K. Saito, K. Watanabe, Y. Ushiku, and T. Harada, Maximum classifier discrepancy for unsupervised domain adaptation, in *2018 IEEE/CVF Conference on Computer Vision and Pattern Recognition* (IEEE, New York, 2018), pp. 3723–3732.

[63] J. Jiang, Y. Ji, X. Wang, Y. Liu, J. Wang, and M. Long, Regressive domain adaptation for unsupervised keypoint detection, in *Proceedings of the IEEE/CVF Conference on Computer Vision and Pattern Recognition* (IEEE, New York, 2021), pp. 6780–6789.

[64] G. E. Dahl, D. Yu, L. Deng, and A. Acero, Context-dependent pre-trained deep neural networks for large-vocabulary speech

recognition, IEEE Trans. Audio Speech Lang. Process. **20**, 30 (2012).

[65] L. Deng, M. L. Seltzer, D. Yu, A. Acero, A.-r. Mohamed, and G. Hinton, Binary coding of speech spectrograms using a deep auto-encoder, in *Eleventh Annual Conference of the International Speech Communication Association (INTERSPEECH 2010)* (ISCA, Makuhari, Chiba, Japan), pp. 1692–1695.

[66] W. Ouyang, X. Wang, X. Zeng, S. Qiu, P. Luo, Y. Tian, H. Li, S. Yang, Z. Wang, C.-C. Loy *et al.*, DeepID-net: Deformable deep convolutional neural networks for object detection, in *Proceedings of the IEEE Conference on Computer Vision and Pattern Recognition* (IEEE, New York, 2015), pp. 2403–2412.

[67] Z.-Q. Zhao, P. Zheng, S.-T. Xu, and X. Wu, Object detection with deep learning: A review, IEEE Trans. Neural Networks Learn. Syst. **30**, 3212 (2019).

[68] K. Lin, T. H. Li, S. Liu, and G. Li, Real photographs denoising with noise domain adaptation and attentive generative adversarial network, in *Proceedings of the IEEE/CVF Conference on Computer Vision and Pattern Recognition Workshops* (IEEE, New York, 2019), pp. 1717–1721.

[69] S. Kumar Giri, U. Saalmann, and J. M. Rost, Purifying electron spectra from noisy pulses with machine learning using synthetic Hamilton matrices, Phys. Rev. Lett. **124**, 113201 (2020).

[70] A.-T. Le and C. Lin, Polarisation states of high harmonic generation from aligned molecules, J. Mod. Opt. **58**, 1158 (2011).

[71] P.-C. Huang, C. Hernández-García, J.-T. Huang, P.-Y. Huang, C.-H. Lu, L. Rego, D. D. Hickstein, J. L. Ellis, A. Jaron-Becker, A. Becker, S.-D. Yang, C. G. Durfee, L. Plaja, H. C. Kapteyn, M. M. Murnane, A. H. Kung, and M.-C. Chen, Polarization control of isolated high-harmonic pulses, Nat. Photonics **12**, 349 (2018).

[72] D. D. Hickstein, F. J. Dollar, P. Grychtol, J. L. Ellis, R. Knut, C. Hernández-García, D. Zusin, C. Gentry, J. M. Shaw, T. Fan *et al.*, Non-collinear generation of angularly isolated circularly polarized high harmonics, Nat. Photonics **9**, 743 (2015).

[73] T. Fan, P. Grychtol, R. Knut, C. Hernández-García, D. D. Hickstein, D. Zusin, C. Gentry, F. J. Dollar, C. A. Mancuso, C. W. Hogle *et al.*, Bright circularly polarized soft x-ray high harmonics for x-ray magnetic circular dichroism, Proc. Natl. Acad. Sci. USA **112**, 14206 (2015).

[74] G. Lambert, B. Vodungbo, J. Gautier, B. Mahieu, V. Malka, S. Sebban, P. Zeitoun, J. Luning, J. Perron, A. Andreev *et al.*, Towards enabling femtosecond helicity-dependent spectroscopy with high-harmonic sources, Nat. Commun. **6**, 6167 (2015).

[75] C. Zhai, R. Shao, P. Lan, B. Wang, Y. Zhang, H. Yuan, S. M. Njoroge, L. He, and P. Lu, Ellipticity control of high-order harmonic generation with nearly orthogonal two-color laser fields, Phys. Rev. A **101**, 053407 (2020).